CHEMISTRY OF MATERIALS

pubs.acs.org/cm

Article

Thermally Stable Binary Two-Dimensional Hybrid Organic–Inorganic Perovskite Glasses

Arad Lang,* Chumei Ye, Celia Chen, Lauren N. McHugh, Emily V. Shaw, Catherine Dejoie, Giulio I. Lampronti, Malvina Constantinou, Rachel C. Evans, Thomas D. Bennett, and Siân E. Dutton

Cite This: *Chem. Mater.* 2025, 37, 8809–8821

Read Online

ACCESS | Metrics & More | Article Recommendations | Supporting Information

ABSTRACT: Two-dimensional hybrid organic–inorganic perovskites (2D HOIPs) are promising candidates for next-generation optoelectronics. Unlike their three-dimensional counterparts, many 2D HOIPs can melt upon heating. Careful structural engineering may suppress their crystallization upon cooling, yielding a melt-quenched glassy phase. These "HOIP glasses" exhibit short-range order similar to that of their crystalline counterparts but lack long-range order. Although these novel hybrid glasses have garnered scientific interest, they are thermally unstable and revert to their crystalline form within minutes to days. In this study, we demonstrate the preparation of thermally stable 2D HOIP glasses using melt alloying—a technique traditionally employed in metallurgy. By blending and comelting two types of glass-forming 2D HOIP powders, namely $(S\text{-NEA})_2PbBr_4$ (*S*-NEA = (*S*)-(−)-1-(1-naphthyl)ethylammonium) and $(MIPA)_2PbI_4$ (MIPA = *N*-methyliodopropylammonium), we form binary glasses with composition-dependent bond lengths as well as thermal and physical properties, including glass transition temperature (T_g), optical band gap (E_g), and mechanical hardness (H). Notably, owing to changes in recrystallization enthalpy and entropy, these binary glasses demonstrate a much lower tendency to recrystallize, with the one containing 40 mol % $(MIPA)_2PbI_4$ remaining amorphous for as long as six months. This enhanced thermal stability paves the way for potential long-term applications of this emerging class of functional hybrid glasses.

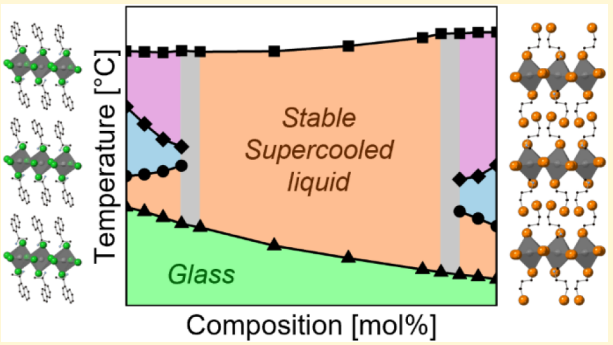

INTRODUCTION

The hybrid organic–inorganic perovskite (HOIP) family comprises dozens of different structures, among them are the hybrid metal-halide perovskites (MHPs).[1] These materials are at the center of current optoelectronic research, as they demonstrate significant potential for use in applications such as photovoltaics (PVs),[2−5] light-emitting diodes (LEDs),[6−9] and photodetectors.[10−13] Three-dimensional (3D) MHPs adopt the perovskite ABX_3 structure, where A^+ is a small organic cation (e.g., methylammonium, MA^+, or formamidinium, FA^+), B^{2+} is a metal cation (typically Pb^{2+} or Sn^{2+}), and X^- is a halide (Cl^-, Br^- or I^-). The inorganic ions (B^{2+} and X^-) form a 3D network of corner-sharing $[BX_6]^{4-}$ octahedra, with the A^+ cations occupying the free spaces between them.[14,15] The crystal structure of the 3D HOIPs is determined by the Goldschmidt tolerance factor, which accounts for the effective sizes of the three components (A^+, B^{2+}, and X^-).[16]

To further increase the structural diversity of HOIPs, the small organic cation (A^+) can be replaced with a bulkier one. Such substitution breaks the tolerance factor limitations and induces the formation of low-dimensional HOIP phases.[17−19] One of these phases is the two-dimensional (2D) Ruddlesden–Popper (RP) MHP phase, with the chemical formula $A_{n+1}B_nX_{3n+1}$. Here, n represents the number of inorganic layers, formed by corner-sharing $[BX_6]^{4-}$ octahedra, and separated by organic bilayers.[20] These 2D HOIPs were shown to possess enhanced performance stability,[21,22] which, together with their band gap tunability[23,24] and simple synthesis routes,[25−27] makes them promising candidates to replace their 3D counterparts.[28] One property, induced by the layered structure described above, is the ability of these 2D HOIPs to undergo melting, i.e., a thermally induced solid-to-liquid transformation.[29] Such meltability is prominent in single-layered RP HOIPs (n = 1, A_2BX_4) and has not yet been observed in 3D MHPs.[30] However, it has been observed in 3D HOIPs with the chemical formula $[TPrA]M(dca)_3$ (where TPrA = tetrapropylammonium, M = Mn, Fe, or Co, and dca = dicyanamide).[29,31,32] The melting temperature (T_m) of the 2D HOIPs, typically occurring in the range of 100–200 °C, is determined

Received: July 17, 2025
Revised: October 16, 2025
Accepted: October 16, 2025
Published: October 30, 2025

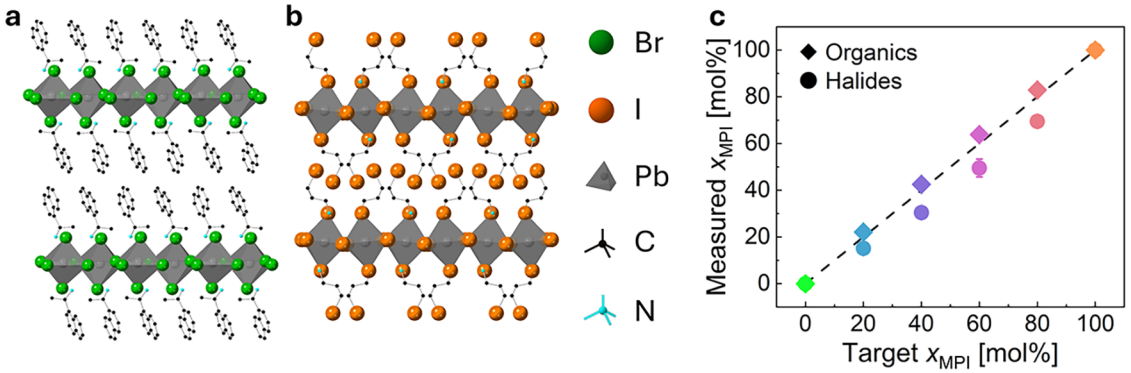

Figure 1. Composition of the crystalline blends: Crystal structures of (a) $(S\text{-NEA})_2PbBr_4$ and (b) $(MIPA)_2PbI_4$, as obtained from Rietveld refinement against the corresponding HR-PXRD data. The colors of the atoms are as follows: green—Br; orange—I; gray—Pb; black—C; cyan—N. Hydrogen atoms were omitted for clarity. (c) The molar concentration of MPI crystals in each blend, as was calculated based on organics (diamonds) and halides (circles) determination, using ^{1}H NMR and SEM-EDS, respectively.

by the structure and composition of both the inorganic[33,34] and the organic parts.[34−38]

While the vast majority of 2D HOIPs are crystalline, a select few have recently been shown to form a glassy (amorphous) structure.[29,36,39,40] These so-called "HOIP glasses" can be prepared by the synthesis of the crystalline form, followed by melt-quenching[36,39] or mechanical milling.[41] Upon glass formation, the HOIPs lose their long-range order, while retaining some short-range order.[42] Such structural alterations induce changes in the physical properties of the HOIP, as both the optical band gap and Young's modulus of the HOIP glasses have been shown to be affected.[39,43,44]

One of the main characteristics of these glasses is their structural thermal instability, i.e., their tendency to revert to their crystalline form upon mild heating.[39,45] Here, "thermal stability" will henceforth refer specifically to the ability of HOIP glasses to resist recrystallization upon heating. To date, no MHP system is known to be able to form a thermally stable, or nonrecrystallizing, HOIP glass. Instead, all known MHP glasses were shown to transform to their thermodynamically stable crystalline phase, even at room temperature, within minutes to days.[30,45] Such structural tunability can be beneficial for applications that require switching abilities.[46] However, it prevents the glassy HOIPs from being integrated into other glass-based applications,[30,47] such as optical fibers,[48,49] thermoelectrics,[50,51] and all-perovskite crystal-glass optoelectronic composites,[52,53] which require long-term stability of the material's physical properties and, by extension, its structure.

Here, we address the issue of HOIP glasses' poor thermal stability by employing melt alloying and forming binary glasses. This practice, also known as liquid phase blending, involves mixing the pure materials, usually in powder form, followed by comelting and subsequent cooling.[54,55] As was previously demonstrated for other hybrid systems, including coordination polymers (CPs),[56] metal−organic frameworks (MOFs),[57] and 2D HOIPs,[58] such melt alloying allows tuning of the physical properties. In this work, we study the blend of the two known-to-date glass-forming 2D HOIPs, namely $(S\text{-NEA})_2PbBr_4$ (*S*-NPB; *S*-NEA = (*S*)-(−)-1-(1-naphthyl)ethylammonium)[39] and $(MIPA)_2PbI_4$ (MPI; MIPA = *N*-methyliodopropylammonium, 3-iodo-*N*-methylpropan-1-ammonium).[36] After synthesizing their crystalline powders, we blended them at different ratios, then melt-quenched the blends to form binary HOIP glasses with different compositions. The resulting glasses were shown to possess composition-dependent properties: their glass transition temperature (T_g), mechanical hardness (H), and optical band gap (E_g) all gradually changed with the blending ratio. Moreover, X-ray total scattering has revealed that bonds within the $[PbX_6]^{4-}$ octahedra (X = Br and/or I), which remain upon glass formation, also change with composition. Most importantly, due to thermodynamic effects, namely, a reduction in the magnitude of recrystallization enthalpy and entropy, the binary glasses exhibit enhanced thermal stability, as their recrystallization is significantly delayed. Specifically, the glass containing 40 mol % MPI was shown to be thermodynamically stable, a result further supported by the absence of Bragg peaks in its X-ray diffraction patterns over six months of measurements.

RESULTS AND DISCUSSION

We have synthesized the pure crystalline 2D HOIPs in powder form, based on previously reported procedures (see Experimental Section for full details),[36,39] and prepared blends by mixing different ratios of the powders (see Table S1). The structures of the 2D HOIPs are presented in Figure 1a,b (the molecular structure of the organic cations is presented in Figure S1). The crystalline structures, as well as the purity of each HOIP, were refined by Rietveld refinement against the high-resolution powder X-ray diffraction (HR-PXRD) patterns, as collected in ID22 of the European Synchrotron Radiation Facility (ESRF; see Experimental Section for more details and Figure S2 for refinement results).

For simplicity, each sample will be named according to the molar ratio of its MPI content (for example, the sample named 20% is the one with x_{MPI} = 20 mol % and $x_{S\text{-NPB}}$ = 80 mol %). The two blended 2D HOIPs differ from one another in the molecular structure of their organic cation (A^+), as well as the identity of their halide (X^-). Hence, the true blend composition can be calculated by determining the relative concentration of the MIPA molecules and of the I atoms, using hydrogen nuclear magnetic resonance (^{1}H NMR) and energy dispersive spectroscopy in the scanning electron microscope (SEM-EDS), respectively. The excellent correlation between the target and measured concentrations of the 2D HOIPs in each blend, as shown in Figure 1c, indicates well-mixed samples (see SEM-EDS spectra in Figure S3 and ^{1}H NMR spectra in Figures S4 and S5). This was further corroborated using X-ray diffraction (XRD), as the normalized integrated intensity of the (020) reflection of the MPI crystals in the

https://doi.org/10.1021/acs.chemmater.5c01893
Chem. Mater. 2025, 37, 8809−8821

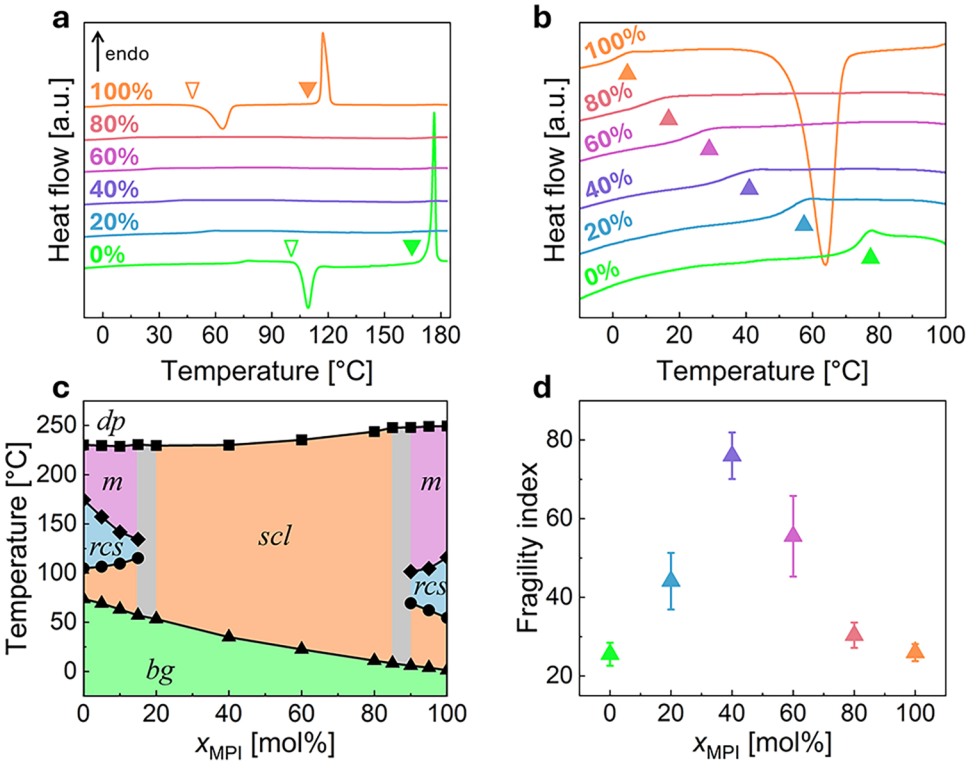

Figure 2. Thermal behavior of the *S*-NPB:MPI binary glasses: (a) DSC heating scan of the glasses, performed after melt-quenching of the HOIP blends. (b) A zoom-in on the composition-dependent glass transition temperatures of the binary glasses. The symbols on the DSC scans in (a,b) represent as follows: empty down-facing triangles—glass recrystallization (T_x); filled down-facing triangles—crystal melting (T_m); filled up-facing triangles—glass transition (T_g). (c) A $T-X$ diagram for the binary glasses, constructed based on their DSC heating scans. The diagram indicates the possible state of matter according to the glass composition and temperature, as follows: green—binary glass (*bs*); orange—supercooled liquid (*scl*); blue—recrystallized solid (*rcs*); purple—melt (*m*); white—decomposition products (*dp*). The black lines represent phase transitions, with the data points shaped as follows: triangles—glass transition; circles—recrystallization; rhombuses—melting; squares—decomposition. The gray rectangles represent border areas. (d) Fragility index of the glass-forming binary liquids.

blend closely follows the expected rational first-degree trend[59] (Figure S7).

To study the thermal behavior of the blends, we employed thermal gravimetric analysis (TGA) and scanning differential calorimetry (DSC). The first DSC heating scan is presented in Figure S8a. For the pure *S*-NPB and MPI crystals, we measured melting temperatures of 177 and 118 °C, respectively. These values are in good agreement with the previously reported ones.[36,39] As expected based on our previous work,[58] the melting temperature of the blends is lower than either of the individual components. Figure S8b presents a temperature vs composition ($T-X$) diagram, constructed based on the thermal behavior of the blends during the first heating stage, as measured by DSC and TGA (see Figure S8c). Before decomposition, the blends can be in one of two states: a crystalline blend (at low T), or a melt (at higher T).

After melting the blends, we cooled down the samples to −30 °C. The DSC curves recorded during the cooling stage were featureless, as expected (see Figure S8c,d), since no crystallization occurred. Instead, binary HOIP glasses were formed. The comparison between the XRD patterns of the samples before and after melting, confirming the glass formation, is presented in Figure S9. This is further supported by the FT-IR spectra of the glasses (Figure S5), which reveal the emergence of a high-energy broad peak associated with N−H stretching of unbound amino groups,[42] while the low-energy organic peaks remain largely unchanged. The similarity of the ^{1}H NMR spectra before and after vitrification (Figures S5 and S6) confirms that the organic cations are preserved during melt-quenching. Notably, the formation of methyl-bromopropylammonium (MPBA)[60,61] is indicated by an additional peak, highlighted in blue in Figure S5. This peak is observed in all of the blended samples but is absent in the pure HOIPs (0% and 100%). As its intensity remains essentially unchanged upon glass formation, this feature appears to be a blend-induced phenomenon.

Next, the samples were heated once again, this time in their glassy state. The DSC traces recorded during the second heating stage are presented in Figure 2a. During the heating of the glasses, they undergo a glass transition (Figure 2b). For the pure *S*-NPB and MPI, we measured glass transition temperatures (T_g) of 74 and 1 °C, respectively. Once again, these values are in excellent agreement with the previously reported ones.[36,39] Notably, T_g changes according to the glass composition (indicated by up-facing filled triangles in Figure 2b).

Upon further heating, the pure HOIP glasses transform back to their thermodynamically stable crystalline form. This recrystallization is manifested as an exothermic peak in the DSC trace and is indicated by empty triangles in Figure 2a. Surprisingly, this peak is absent in all of the binary glasses. The absence of the recrystallization peak suggests that the hybrid glasses are thermally stable. This is further corroborated by the lack of the melting peak (down-facing filled triangles in Figure 2a), as the binary glasses do not melt.

https://doi.org/10.1021/acs.chemmater.5c01893
Chem. Mater. 2025, 37, 8809−8821

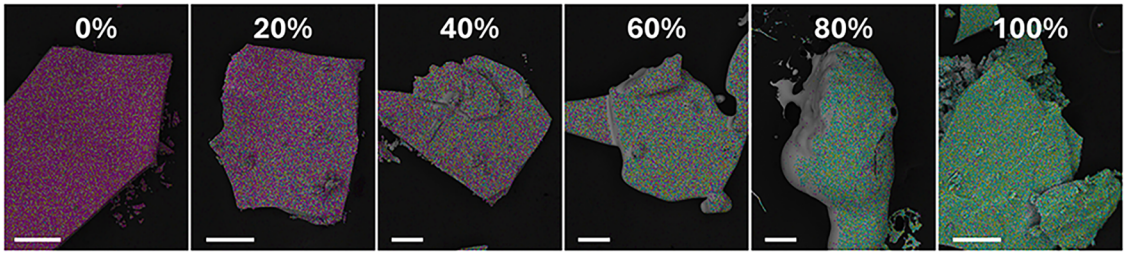

Figure 3. Chemical analysis of the *S*-NPB:MPI binary glasses: EDS elemental maps of the binary glasses (after melting). The color of each element is as follows: Pb—yellow; Br—magenta; I—cyan. Scale bars: 250 μm.

The $T-X$ diagram, constructed based on the DSC heating scan of the binary glasses, is presented in Figure 2c. The low ($x_{MPI} \leq 15$ mol %) and high ($x_{MPI} \geq 90$ mol %) concentration binary glasses, as well as the pure HOIP glasses, can be found in one of four states, according to their temperature: a binary glass (*bs*), a supercooled liquid (*scl*), a recrystallized solid (*rsc*), or a melt (*m*). Here, *scl* refers to (potentially metastable) a liquid that was formed by crossing the glass transition, while *m* refers to a liquid that was formed by melting a crystal. The transition temperatures between the different states are all composition-dependent (see Figure S3 for more DSC scans). Notably, the intermediate blends (20 mol % $\leq x_{MPI} \leq$ 85 mol %) do not recrystallize when heated. After the glass transition (T_g), the supercooled liquid is stable until decomposition at T_d = 230−250 °C (depending on the glass composition, see Figure S8f).

One crucial property of glasses is the fragility of the glass-forming liquid. Fragility, while not completely understood, can be considered the level of change in viscosity when approaching the glass transition.[62−64] Strong glass formers, such as silicon oxide (SiO_2) and germanium oxide (GeO_2), exhibit a linear and gradual change in viscosity near T_g. In contrast, fragile glass formers, such as triphenylchloromethane (TPCM) and *o*-terphenyl (OTP), exhibit a dramatic change in viscosity, as it drops several orders of magnitude when approaching T_g.[62,64,65] Here, we used DSC to calculate the fragility index, *m* (see Experimental Section for full details).[66] The change in the fragility index with the binary glass composition is presented in Figure 2d. The fragility index for both pure glasses (0% and 100%) is $m \approx 30$. This value is in excellent agreement with the fragility previously reported for *S*-NPB glass,[44] and is in the intermediate range between strong ($m_{SiO_2} = 20$, $m_{GeO_2} = 24$) and fragile ($m_{TPCM} = 93$, $m_{OTP} = 76$) glass formers.[63] Upon blending, the fragility index increases, as the value of *m* reaches a high value of 77 for the 40% binary glass. This suggests that the binary glasses possess a more "molecular-glass-like" behavior.

A noticeable characteristic presented in Figure 2b (and in Figure S14a) is the negative deviation from linearity in T_g when plotted vs the binary glass composition. For random copolymers,[67] such deviation can arise from either of two reasons: (i) enthalpic effects, in the form of repulsive interchain interaction, or (ii) entropic (conformational) effects, in the form of breaking stiff domains. HOIP binary glasses, assumed to be randomly blended, can be considered random (statistical) copolymers (similar to small-molecule binary glasses).[67] To this end, we calculated the change in enthalpy (ΔH_g) and entropy (ΔS_g) during glass transition, according to eqs 1 and 2:[68,69]

$$\Delta H_g = \Delta C_p(T_f - T_i) \quad (1)$$

$$\Delta S_g = \Delta C_p \ln\left(\frac{T_f}{T_i}\right) \quad (2)$$

$$T_g = \Delta H_g / \Delta S_g \quad (3)$$

where T_i and T_f are the onset and offset temperatures of the glass transition, respectively, and ΔC_p is the difference in heat capacity between the glassy and supercooled liquid states. As seen in Figure S14, the calculated values are all positive, as expected. Surprisingly, even though ΔC_p monotonically changes with composition, both ΔH_g and ΔS_g increase in value upon blending. While both stay roughly constant, independent of the binary glass composition, they are always higher for the blends than for the pure glasses. Such an increase can be attributed to a blending-induced enhancement in disorder at the glass transition, possibly due to a broader distribution of transition temperatures or an excess of free volume. Based on this, one can conclude that the overall negative deviation (Figures 2b,c, and S14a), is governed by entropic effects. As was shown before for *S*-NPB glass, stacking of the organic (A-site) cations has a pivotal role in the glass-formation ability of the HOIP.[39] It is possible that the blending and formation of a binary glass interrupts the unique stacking of the *S*-enantiomer cations (which does not exist in the nonglass-forming racemic HOIP),[39] therefore reducing the interactions, hence lowering T_g. Such negative deviation in T_g was demonstrated before for poly(methyl methacrylate-styrene) copolymers (P-MMA-St), where the addition of styrene monomers broke the rigid MMA domains.[67,70] Even though T_g decreases with increasing value of x_{MPI}, as presented in Figure 2c (and Figure S14a), blending also induces a decrease in T_m (Figure S8b). These changes result in an overall increase in the T_g/T_m ratio for the binary glasses, making it further exceed 2/3, and enhancing their so-called "glass-forming ability" (Figure S13).[71,72]

We employed SEM-EDS to study the chemical homogeneity of our binary glasses. Figure 3 presents elemental maps for each sample, layered on the corresponding backscattered electrons (BSE) image (separate images for each signal are presented in Figure S15). All images were taken after melting, thus representing the binary glasses. The one exception is the 100% sample (pure MPI), as in this sample, recrystallization occurs rapidly at room temperature, hence, the image represents the crystalline state. One can clearly observe the gradual change from purple to green, corresponding to the shift from Br-rich to I-rich samples. Moreover, the uniform hue in each sample suggests that the glasses are homogeneous, and no Br- or I-rich domains are present. Such homogeneity was shown to occur in melt-blended HOIPs;[58] however, it did not

https://doi.org/10.1021/acs.chemmater.5c01893
Chem. Mater. 2025, 37, 8809−8821

occur in melt-blended MOFs.[57] Note that SEM-EDS alone cannot rule out the presence of compositional nanodomains in the binary glasses. However, combined with the detection of a single glass transition for each composition (unlike block copolymers,[73] see Figure 2a,b), one can conclude that homogeneity was indeed achieved.

To study the structure of our samples, we performed a total scattering experiment using synchrotron-source X-rays.[74,75] Following data processing, we constructed the X-ray pair distribution function (XPDFs) for our samples. Each sample was measured as a crystalline blend, then underwent *in situ* melt-quenching and measured again at its glassy state (see Experimental Section for full details). Figure 4a presents the XPDF patterns of the crystalline blends (dark curves) and the binary glasses (light curves).

The crystalline blends all demonstrate XPDF peaks across the whole r range. For pure *S*-NPB (0% sample) and MPI (100% sample), the assignment of the main peaks to specific interatomic distances is presented in Figure S16. Since heavy elements are much stronger X-ray scatterers,[76] the XPDF in this case primarily reflects the inorganic interactions, namely, $X-X$ (X = Br or I), Pb−Pb, and Pb−X distances. According to the reported crystal structures,[36,39] the average Pb−X bond in *S*-NPB and MPI is 3.034 Å and 3.206 Å, respectively. This is in excellent agreement with our data. Unfortunately, the XPDF measurements were not sensitive enough to resolve the Pb−Br and Pb−I peaks in the crystalline blends. However, a gradual shift in the position of the first Pb-X peak was observed with an increasing x_{MPI} value, corresponding to the increase in average Pb−X bond length (from Pb−Br to Pb−I).

The low-r region (2.5 Å < r < 7.5 Å, gray area in Figure 4a) of the $D(r)$ curves of the binary glasses (light curves) is almost identical to their corresponding crystalline blends (dark curves). This implies that the short-range order (r < 7.5 Å) of the glasses does not change significantly upon glass formation. The peaks that remain after vitrification correspond to intraoctahedral Pb−X (r = 3.0−3.3 Å) and $X-X$ (r = 4.2−4.5 Å) distances, as well as the Pb−Pb distance between neighboring octahedra (r = 6.2−6.6 Å). For higher r values (r > 7.5 Å), the XPDF patterns of the glasses are all featureless, indicating the loss of the long-range order. This change, expected to occur during glass formation, is also further corroborated by the PXRD patterns, as the Bragg peaks disappear (Figure S9). Such changes in the XPDF and PXRD patterns are similar to those observed before for pure *S*-NPB glass. Structurally, they suggest a short-range connectivity of neighboring lead-halide octahedra; however, with no long-range order.[42,44]

Recently, works by us[44] and by others[42] have studied in detail the structural changes that occur upon glass formation in pure *S*-NPB. As shown, while the long-range order is lost when the crystal undergoes melting and vitrification, the inorganic layered structure is preserved to some extent, as the octahedral units remain connected in a disordered manner. This layered structure gives rise to the broad XRD reflection seen for the pure *S*-NPB glass at $2\theta \approx 6°$ (0% sample, see Figure S17). One possible reason is the molecular rigidity of the naphthyl groups, which prevents the material from completely losing its layered structure.[42] Such a "disordered layered structure" was not observed in pure MPI glass (100%), as no low-angle broad peaks were detected in its XRD pattern. However, it is difficult to determine whether this is due to the flexible alkyl chains in the MIPA molecule or rather to the weak diffraction of the MPI structure (see Figure S17).

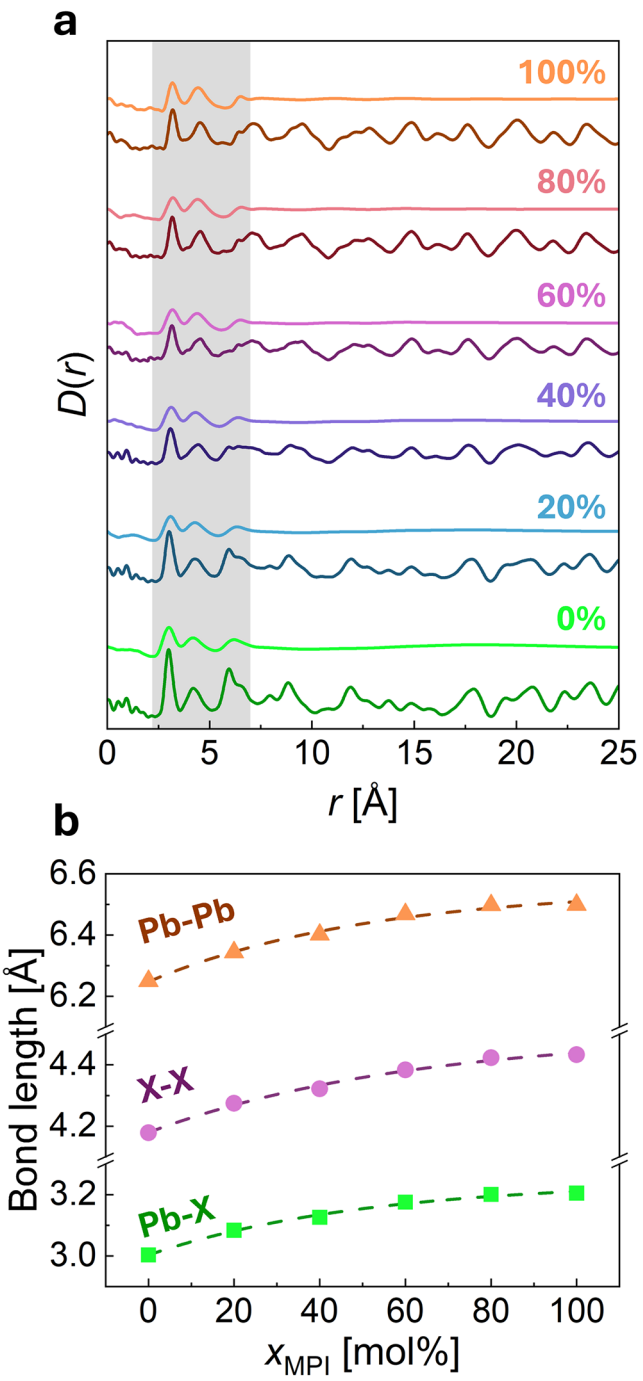

Figure 4. XPDF analysis: (a) $D(r)$ plots of samples with different concentrations. In each pair, the dark curve corresponds to the crystalline blend, while the lighter curve corresponds to the *S*-NPB:MPI binary glass (after *in situ* melt-quenching). The gray area represents the short-range order, which remains largely unchanged after vitrification. (b) Changes in short-range interatomic distances with the binary glass composition. The dashed lines are exponential trend lines, serving as guides for the eye. All error bars in (b) are smaller than the data points.

We have fitted the three short-range XPDF peaks of the binary glasses (Figure S18), and calculated how the corresponding interatomic distances change with composition. The results are presented in Figure 4b. As expected, the more I

https://doi.org/10.1021/acs.chemmater.5c01893
Chem. Mater. 2025, 37, 8809−8821

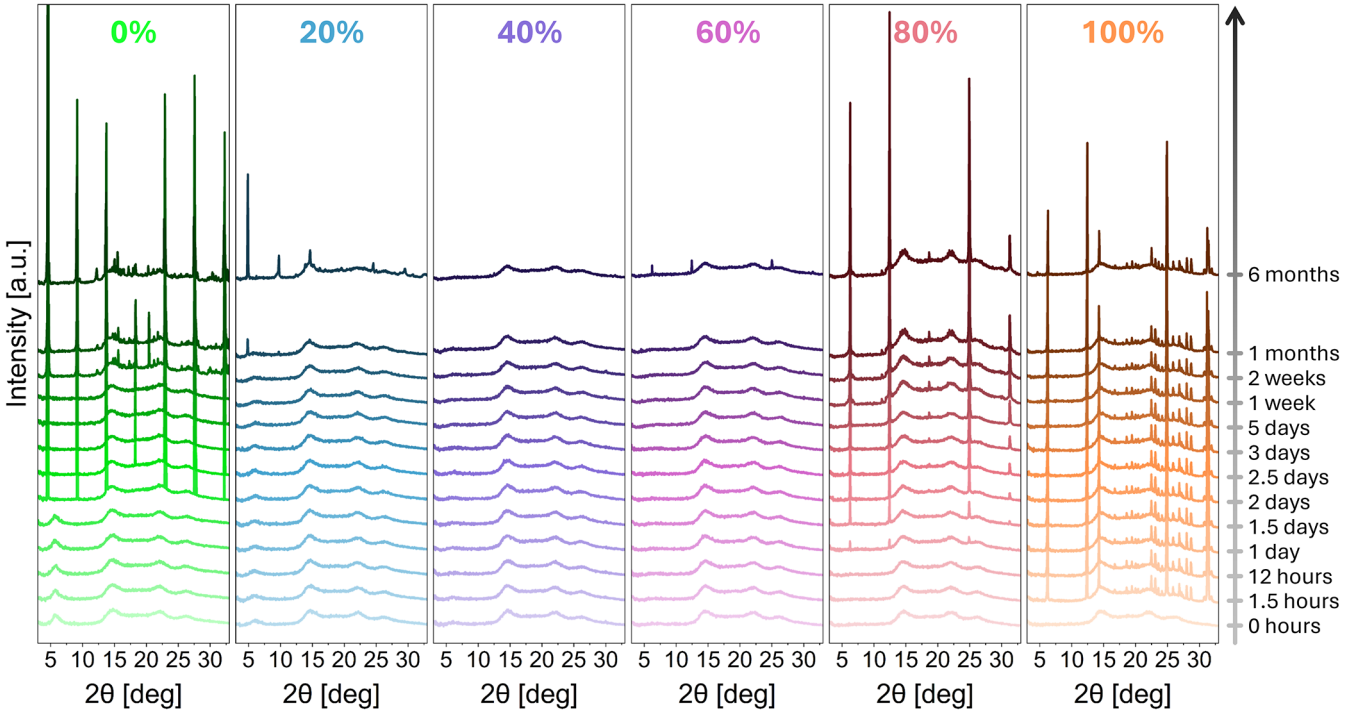

Figure 5. Thermal stability of *S*-NPB:MPI binary HOIP glasses: XRD patterns of each binary glass, recorded over a period of one month, and once again after six months. Each sample comprises a layer of HOIP glass, sandwiched between a microscope glass slide and a Kapton sheet. Darker plots correspond to measurements taken longer after glass formation. The time passed between the formation of the glass and each XRD scan is indicated on the right. The scans are all stacked on one another, and, to emphasize the long-term stability, the last scan is offset to the positive *y*-direction.

(and hence, less Br) is in the glass, all short-range distances expand. Note that the relative elongation in the binary glasses is more pronounced when the distance is originally shorter (Figure S19). For the Pb−*X* bond (i.e., the shortest bond), there is a 6.7% change between the pure *S*-NPB and MPI glasses. After that, the *X*−*X* distance (2nd shortest) changes by 6.1%, while the Pb−Pb distance (3rd shortest), changes only by 4.0% with the binary glass composition.

We have used XRD to assess the blending-induced enhancement in the thermal stability of our binary glasses. We prepared Kapton-covered layers of each composition by melt-quenching them on a glass substrate from 190 °C to room temperature (see Experimental Section for the detailed preparation procedure). Then, we recorded their XRD patterns every few hours over a period of one month, and once more after six months (see Experimental Section for a full description). The resulting diffractograms are presented in Figure 5. In each panel, the lightest plot represents the as-is glass, i.e., immediately after melt-quenching. In this stage, the samples are all completely amorphous, and no Bragg reflections originating from the crystalline HOIPs are present. The only visible features are the broad Kapton reflections (around $2\theta \approx 15°$, 22°, and 26°, see Figure S9). Additionally, for the *S*-NPB-rich samples (0% and 20%), the characteristic broad reflection of the glass[39,42,44] is seen at $2\theta \approx 6°$.

After 90 min, the samples all maintain their glassy structure. The only exception is the pure MPI, which demonstrates a crystalline structure with distinct Bragg peaks. For the pure MPI glass, the measured glass transition is well below room temperature, and its recrystallization temperature is not much higher (T_g = 1 °C and T_x = 54 °C, see Figure 2d). This allows the glass sufficient thermal energy and dynamic flexibility to revert quickly to its thermodynamically stable crystalline form. Upon recrystallization, the diffraction peaks appear narrow and sharp already at this point, and do not change, neither in intensity nor shape, in the subsequent scans, suggesting an immediate and rapid recrystallization process.

The next sample to recrystallize is 80%, after 1 day. This sample is the MPI-richest binary glass. Here, compared to the pure MPI, the first Bragg peaks appear broad and weak, and their intensity increases over time. Such behavior indicates a more gradual recrystallization. When comparing the diffraction patterns of the recrystallized 80% and 100% samples, one can notice that the high-intensity peaks appear in similar positions. This suggests that the 80% sample recrystallizes in the MPI structure. Not long after (1.5 days), the pure *S*-NPB glass (0%) recrystallizes as well. Here, similarly to the pure MPI glass and as expected from a pure material, the recrystallization is abrupt, and the Bragg reflections immediately appear sharp and intense. Upon recrystallization, the broad reflection at $2\theta \approx 6°$, which is characteristic of the *S*-NPB glass,[39,42,44] disappears (see also Figure S17).

After one month under ambient conditions, the 20% sample slowly begins to recrystallize, as indicated by the weak XRD peak at $2\theta \approx 5°$. This recrystallization continues, as more peaks are visible after 6 months. By this time, the 60% sample also demonstrates slight recrystallization. These samples (20% and 60%), as well as the previously recrystallized 80% glass, did not recrystallize in the DSC. This contradiction can be resolved when considering the different thermal conditions (isothermal ambient conditions for the XRD experiment, vs constant heating rate in the DSC scans), which affect the recrystallization kinetics. Strikingly, for the 40% sample, no Bragg peaks

https://doi.org/10.1021/acs.chemmater.5c01893
Chem. Mater. 2025, 37, 8809−8821

appear even after 6 months. This suggests that the 40% binary glass is inherently thermally stable at room temperature.

To explain these results, we used DSC to extract thermodynamic coefficients and calculate $\Delta G_x(x_{MPI})$, i.e., how the Gibbs free energy of recrystallization (at room temperature) changes with the composition of the binary glasses (see full description in the Supporting Information). According to our calculations, $\Delta G_x < 0$ for $x_{MPI} < 21.3 \pm 0.2$ mol %, and for $x_{MPI} > 64 \pm 4$ mol %. This means that in these regions, recrystallization is thermodynamically favored, even though it can take a long time to occur (like in the 20% sample). However, for binary glasses with a composition between these values (21.3% < x_{MPI} < 64%), $\Delta G_x > 0$, and recrystallization at room temperature is thermodynamically unfavored. This simple thermodynamic treatment overlooks kinetic effects, such as structural relaxation of the glass[77] or possible multistep transformations.[78] Most importantly, it treats the glass as if it were an equilibrium phase, regardless of it being a metastable state by definition.[48,79,80] Despite that, our model explains well the absence of recrystallization observed for the 40% sample, which is deep inside the "thermally stable" composition region. However, the XRD patterns collected after 6 months (darkest plots in Figure 5) do present (slight) recrystallization of the 60% sample, which, according to our model, should be thermally stable. As this composition is very close to the upper limit of the stability region (64 mol %), small fluctuations in this composition across the bulk sample (e.g., due to possible structural[81] or light-induced[82,83] halide segregation) might initiate recrystallization.

The binary HOIP glasses demonstrate long-term stability, which opens the door for integration in a wide variety of applications. Hence, we study how their composition affects several selected physical properties. First, we studied the mechanical properties of the HOIP glasses using nanoindentation,[84,85] and calculated the hardness and Young's modulus of each sample. Each value was calculated as an average of 15 measurements, at different positions in the sample, while the indenter tip was cleaned between each measurement (see Experimental Section for full details). Unfortunately, the use of a standard nanoindenter cannot be employed for soft materials, so only samples with T_g higher than room temperature (i.e., $x_{MPI} \leq 60$ mol %) could be measured. The load vs depth plots are presented in Figure S21.

The hardness (H) of the binary glasses is strongly affected by their composition. As presented in Figure 6a, the binary glasses become softer as the fraction of MPI in the blend increases. This change appears to be linear. The change in hardness can be directly correlated with the reduction in T_g (Figure S14a), as the glasses become softer when the ratio T/T_g approaches 1. In contrast, the Young's modulus (E) of the glasses is not affected by compositional changes (see Figure 6b), as for all of the samples it equals roughly 7 GPa. This value is higher than that of the pure crystal ($E \approx 3$ GPa). This behavior of E may result from the vitrification-induced reduction in the average distance between the inorganic layers (see XRD patterns for the 0% sample in Figure S17),[42] as well as from the possible emergence of 3D connectivity, which potentially increases the interactions. Such dependence of the mechanical properties of the intralayer interaction was previously demonstrated for both organic[86] and inorganic[87] layered materials. These changes do not affect the density of the HOIP, as both the glassy and the crystalline samples were

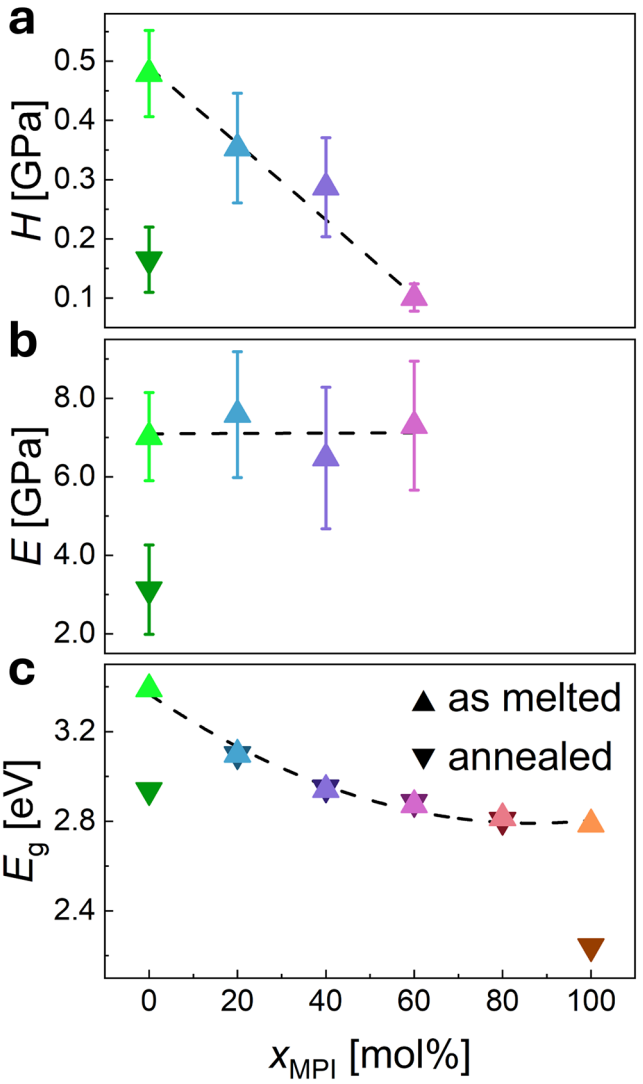

Figure 6. Composition-dependency of physical properties: Effect of the *S*-NPB:MPI binary glass composition on (a) hardness, (b) Young's modulus, both measured using nanoindentation, and (c) optical band gap, calculated based on the UV−vis absorbance spectra and using the Tauc method. Light up-facing triangles represent values measured for melt-quenched glasses, while dark down-facing triangles represent measurements performed after annealing (5 min at 100 °C). The dashed black lines in (a) and (b) represent a linear fit, while in (c) a quadratic fit.

shown to possess a true density of $\rho_{true} = 2.05$ g cm^{-3} (see Figure S22 for pycnometry results). This value is very close to the density calculated based on the *S*-NPB crystal structure, $\rho_{calc} = 2.14$ g cm^{-3}. It is possible that the disorder that occurs during vitrification, such as the weakening of organic−inorganic interactions (as shown in the FT-IR spectra in Figure S10), compensates for the reduction in interlayer distance, thereby maintaining the overall density unchanged.

Finally, as Pb-based MHPs are used for optoelectronic applications, we investigated how the optical band gap of the binary glasses changes with composition. To this end, we employed ultraviolet−visible range (UV−vis) absorbance spectroscopy and used the Tauc method[88,89] to calculate the optical band gap of each sample. The calculated band gaps are presented in Figure 6c (as the UV−vis absorbance spectra and corresponding Tauc plots are presented in Figure S20a,b). The

https://doi.org/10.1021/acs.chemmater.5c01893
Chem. Mater. 2025, 37, 8809−8821

band gap gradually changes between the values of the pure HOIP glasses, a behavior which further corroborates the homogeneity of the glass. Fitting this change to a quadratic equation with the form:[90−92]

$$E_g(x_{MPI}) = x_{MPI}E_{g,MPI} + (1 - x_{MPI})E_{g,S\text{-}NPB} - x_{MPI}(1 - x_{MPI})b \quad (4)$$

gives a bowing parameter of $b = 0.78 \pm 0.07$ eV. This value is relatively high compared to previously reported systems (e.g., $b_{MAPb(Br,I)3} = 0.30$ eV;[93] $b_{Zn(S,Se)} = 0.60$ eV[94]). Such a high value suggests a strong discrepancy between the two pure HOIP glasses, mainly due to the differences in their atomic and molecular components.[92]

After a mild thermal annealing (5 min at 100 °C), a significant drop was recorded for the pure glasses (dark down-facing triangles in Figure 6c), as expected when the HOIP glasses are recrystallized.[39,58] However, the band gap of the hybrid glasses did not change, suggesting no recrystallization has occurred (as was also verified using XRD, see Figure S20c). This further corroborated our previous result, demonstrating that the enhanced structural stability is also accompanied by functional stability.

CONCLUSIONS

In this work, we address a major limitation of two-dimensional hybrid organic−inorganic perovskite (2D HOIP) glasses, that is, their poor thermal stability. This inherent tendency of these glassy materials to recrystallize rapidly into their thermodynamically favored crystalline forms has restricted their utility across optoelectronic and other functional domains.

To overcome this, we employed a melt alloying approach. To this end, we melt-quenched mixtures of two glass-forming 2D HOIPs, namely $(S\text{-NEA})_2PbBr_4$ (*S*-NPB) and $(MIPA)_2PbI_4$ (MPI), to create stable binary HOIP glasses. Differential scanning calorimetry revealed tunable glass transition temperatures that deviate slightly from linearity, likely due to entropic mixing effects. The resulting binary glasses exhibited increased glass-forming fragility relative to their pure counterparts, suggesting more molecular-glass-like behavior. Compositional tuning was also shown to influence their mechanical hardness and optical band gaps, while their Young's moduli remained largely invariant. Synchrotron-based X-ray total scattering measurements confirmed that while long-range order was lost upon vitrification, the short-range structural motifs—specifically the short Pb−*X*, *X*−*X*, and Pb−Pb distances—were largely preserved and systematically evolved with composition. EDS elemental mapping verified the compositional homogeneity of the glasses.

To assess the glasses' long-term thermal stability, we combined X-ray diffraction measurements together with calorimetric-based thermodynamic modeling. Unlike the pure HOIP glasses, which demonstrated rapid recrystallization, the binary systems exhibited significantly suppressed recrystallization behavior. Notably, the glass containing 40 mol % MPI remained fully amorphous after six months at room temperature. Our simple thermodynamic analysis, considering the changes in the Gibbs free energy of recrystallization with composition ($\Delta G_x(x_{MPI})$), showed that for this composition, this change is positive, indicating that recrystallization is thermodynamically disfavored.

Altogether, this work demonstrates, for the first time, the formation of long-term thermally stable 2D HOIP glasses. The combination of stability, tunable properties, and retained short-range order establishes these materials as promising candidates for future applications in optoelectronics, sensing, and energy devices, where stability and design flexibility are essential. Importantly, the method of melt-alloying presented here is straightforward, as it relies only on powder blending and comelting, which makes it readily scalable and reproducible. Nevertheless, this study establishes the feasibility of forming thermally stable HOIP glasses, and further work is required to adapt these materials for common processing and fabrication approaches, such as thin films or fibers. Moreover, as members of the HOIP family, these glasses continue to share some of the intrinsic limitations of their crystalline counterparts, including potential environmental sensitivity and a tendency for halide exchange, which must also be addressed before device integration. Overall, this work establishes a new strategy for stabilizing HOIP glasses, opening a pathway toward their practical use.

EXPERIMENTAL SECTION

$(S\text{-NEA})_2PbBr_4$ Synthesis. *S*-NPB crystals were synthesized based on the procedure reported by Singh et al.[39] In a conical flask, 0.9 g lead(II) bromide ($PbBr_2$, ≥ 98%, Sigma-Aldrich) was dissolved in a mixture of 15 mL concentrated hydrobromic acid (HBr, 48% wt., Thermo Scientific) and 35 mL deionized water. After complete dissolution, 0.78 mL of (*S*)-(−)-1-(1-naphthyl)ethylamine (*S*-NEA, 99%, Thermo Scientific) was added to the solution (while vigorously stirring), followed by sealing the flask and heating it to 90 °C (in a silicone oil bath). The flask was left at this temperature for 3 h. Then, the stirring was turned down (100 rpm), and the heating was turned off completely. The flask was left to cool down naturally to room temperature, in the oil, overnight, and a white-yellowish powder was formed upon cooling. The solution, containing the *S*-NPB powder, was transferred to a Falcon tube and was centrifuged (3000 rpm, 5 min) to dispose of the solvent. Then, 15 mL of diethyl ether (Et_2O, ≥99.8%, Sigma-Aldrich) was added to the tube, shaken well, and centrifuged again. This process was repeated twice more. Finally, the tube was left to dry overnight under vacuum at room temperature.

$(MIPA)_2PbI_4$ Synthesis. MPI crystals were synthesized based on the method reported by Wang et al.[36] in a conical flask, 2.881 g lead(II) iodide (PbI_2, 99%, Aldrich) was dissolved in 50 mL concentrated hydroiodic acid (HI stabilized, 57% at., Thermo Scientific). After complete dissolution, 1.185 mL of 3-(methylamino)-propan-1-ol (MOPA, Fluorochem) was added to the solution (while stirring), followed by sealing the flask and heating it to 90 °C (in a silicone oil bath). The flask was left at this temperature for 48 h. Then, the stirring was turned down (100 rpm), and the heating was turned off completely. The flask was left to cool down naturally to room temperature, in the oil, overnight, and a deep red powder was formed upon cooling. The solution, containing the MPI powder, was transferred to a Falcon tube and was centrifuged (3000 rpm, 5 min) to dispose of the solvent. Then, 15 mL of diethyl ether (Et_2O, ≥99.8%, Sigma-Aldrich) was added to the tube, shaken well, and centrifuged again. This process was repeated twice more. Finally, the tube was left to dry overnight under vacuum at room temperature.

Powder Blending. The desired amounts of *S*-NPB and MPI powders were weighed and transferred to an Eppendorf tube (see Table S1 for quantities). Tubes containing one powder (i.e., only *S*-NPB or only MPI) were also prepared. All tubes were placed on an automatic roller and left to blend overnight. This blending method was proven to produce well-mixed blends.[58]

Halides Determination. Around 1 mg of each sample was mounted on a stainless-steel stab covered with conductive carbon tape. The stabs were inserted into the scanning electron microscope (SEM, Zeiss Gemini), and measured using energy-dispersive X-ray spectroscopy (EDS). To gain statistical information, all measurements were performed at low magnifications (X50). The average atomic

https://doi.org/10.1021/acs.chemmater.5c01893
Chem. Mater. 2025, 37, 8809−8821

concentrations of Br, I, and Pb were calculated based on three measurements taken in different areas, and the error was taken as the standard deviation between them. Then, MPI fraction in the blend was calculated according to (eq 5):

$$x_{\mathrm{MPI}} = \frac{n_{\mathrm{I}}/6}{n_{\mathrm{I}}/6 + n_{\mathrm{Br}}/4} \tag{5}$$

where n_{I} and n_{Br} are the concentrations of I and Br, respectively (in mol %).

^{1}H Nuclear Magnetic Resonance. ^{1}H NMR measurements were performed using a Bruker AVIII 400 MHz spectrometer. ∼20 mg of each sample were transferred to a glass vial (3 mL in volume). The glassy samples were then placed on a hot plate, preheated to 190 °C, until complete melting was achieved, then removed from the hot plate and left to naturally cool down to room temperature. For the crystalline blends, this melting stage was skipped. Then, 0.7 mL of DMSO-d_6 were added to each vial. The vials were sealed and vigorously shaken for a few minutes until the solid had completely dissolved. Each solution was transferred to a standard B25 NMR tube, sealed, and scanned. Data analysis was performed in the MestReNova software. Prediction, assignment, and integration of the peaks were done after automatic background and phase corrections. The MPI fraction (both in the crystalline blends and in the binary glasses) was calculated based on the integration of selected peaks of each organic cation, according to

$$x_{\mathrm{MPI}} = \frac{I_{\mathrm{MPI}}/N_{\mathrm{MPI}}}{I_{\mathrm{MPI}}/N_{\mathrm{MPI}} + I_{\text{S-NPB}}/N_{\text{S-NPB}}} \tag{6}$$

where I and N are the integral intensity of the peak and the number of H atoms it represents, respectively. As two peaks in each cation were selected for integration (see Figures S4 and S5), the above calculation was done four times for each sample, when the concentration was taken as the average, and the error as its standard deviation.

Thermal Gravimetry. TGA was performed using a simultaneous thermal analyzer (SDT 650, TA Instruments). A few mg of each sample were transferred to an alumina crucible and heated from room temperature to 700 °C at a rate of 10 °C min^{-1}. For the glasses, the samples were heated to 185 °C (10 °C min^{-1}), cooled back down to 30 °C (20 °C min^{-1}), and then, after stabilization, scanned during heating up to 700 °C. All heating and cooling steps were performed under an inert Ar atmosphere.

Differential Scanning Calorimetry. DSC scans were performed using a DSC 2500 instrument (TA Instruments). A few mg of each blend were transferred into an aluminum pan, then sealed with a punched aluminum lid. Each sample was stabilized at −30 °C, then heated to 185 °C and cooled back down to −30 °C, twice. The samples were heated at a rate of 10 °C min^{-1}, while cooled at a rate of 15 °C min^{-1} (due to the instability of the MPI glass). All scans were performed under an inert N_2 atmosphere.

Fragility Measurements. DSC samples were prepared as described above. Each sample was melted at 185 °C, then cooled down and heated back up at different rates: 30, 25, 20, 15 °C min^{-1}, making sure each scan crosses T_g (as calculated based on the initial DSC scan and presented in Figure S2f, see a schematic scan profile in Figure S12a). Then, the fictive temperature T_f was calculated as the onset[66] of a tangential fitting in the DSC software, and the fragility index, m, was calculated based on (eq 5):[64,66]

$$m = -\frac{\partial \log R}{\partial\left(\frac{T_g}{T_f}\right)} \tag{7}$$

where R is the scan rate (in K min^{-1}) in the DSC, T_g is the glass transition (in K, measured at a reference scan rate), and T_f is the fictive temperature (in K, i.e., T_g measured at different R values). The value of the fragility index m was extracted as the slope of the $-\log R$ vs T_g/T_f plot.

Powder X-ray Diffraction. PXRD was performed in a Bruker D8 Advance diffractometer. A few mg of each crystalline blend were mounted on a Si low-background holder and scanned in an angle range of 2θ = 3−40° using a CuK$_\alpha$ radiation (λ = 1.5406 Å). Melt-quenched glasses were scanned on a glass substrate, see the Stability Measurements section below.

X-ray Pair Distribution Function. XPDF was performed at ID22—the high-resolution powder X-ray diffraction beamline of the European Synchrotron Radiation Facility (ESRF) in Grenoble, France.[74,75] A few mg of each crystalline blend were gently ground using a mortar and pestle, loaded into a borosilicate capillary (0.9 mm outer diameter, 0.01 mm wall thickness), sealed using epoxy glue, and mounted onto a brass holder. The total scattering patterns of the samples were recorded by 1000 exposures of 500 ms each, using a PerkinElmer medical X-ray detector, as the beam's energy was set to 66 keV (λ = 0.187796 Å). Temperature control was achieved using a cold-nitrogen-gas Oxford Cryosystems cryostream, using its maximal cooling or heating speed (6 K min^{-1}). Each crystalline blend was measured at 290 K, followed by *in situ* melting at 460 K. After melting was achieved, as verified by the high-temperature scattering pattern, the cryostream was removed and the capillary was left to naturally cool down to room temperature. Meanwhile, the cryostream was reset to 290 K. Upon reaching this temperature, the cryostream was brought back, and the sample, now in its glassy state, was further cooled to 260 K and measured once more. Lastly, the glass was reheated to 290 K and measured once again. Container data (empty borosilicate capillary) was collected at the same temperature sequence, as well as a background ("air") scan at room temperature. The data was processed using the GudRun software.[95] Following background reduction, as well as absorbance and Compton corrections, the scattering factor $S(Q)$ was Fourier transformed to produce the pair distribution function $D(r)$.[96,97]

High-Resolution Powder X-ray Diffraction. HR-PXRD was performed in ID22 of the ESRF. A few mg of each pure HOIP were loaded into a 0.5 mm borosilicate capillary (outer diameter), sealed using epoxy glue, and mounted onto a brass holder. The diffraction pattern of each sample was collected at room temperature using a multianalyzer stage detector, as the X-ray wavelength was 0.37594 Å. To avoid beam damage as much as possible, each sample underwent three fast scans at different positions along the capillary, and the patterns were summed together. Rietveld refinement was performed on TOPAS, using CCDC deposition numbers 2015618 (*S*-NPB) and 2325878 (MPI) as the fitted structures. To account for the nonuniform background of the capillary, an empirical background was measured on an empty capillary of the same size. This was included in the refinement with a scale factor equal to $A + B(2\theta)$, where A and B are refinable parameters, together with a 10th order Chebyshev polynomial function. Molecules were defined as rigid bodies with refinable position and orientation parameters. A single isotropic thermal factor was set for each atomic species. For *S*-NPB, Gaussian and Lorentzian isotropic contributions to peak broadening were adopted for crystallite size and microstrains, respectively. For MPI, the Stephens model for anisotropic microstrain contribution was further adopted.[98] The March−Dollase model for preferred orientation was used on the crystallographic planes (0 0 1) for *S*-NPB. For MPI, preferred orientation was modeled with eighth order spherical harmonics.

Glassy Samples Preparation. Standard microscope glass slides were cut into pieces of ∼2 × 2 cm, followed by cleaning them with ethanol, acetone, and isopropanol. In each cleaning cycle, the glass slides were submerged in the organic solvent, sonicated for 30 min, and then washed extensively. After the last washing cycle, the glasses were left to dry under an ambient atmosphere overnight. To prepare the samples, about 50 mg of each crystalline blend was placed on a clean glass slide and transferred to a hot plate, preheated to 190 °C. The sample was left on the hot plate until it completely melted. Subsequent handling depended on the measurements being performed: (i) remained uncovered, for FT-IR, SEM-EDS, and nanoindentation; (ii) covered with a second glass slide, preheated to the same temperature, for UV−vis spectroscopy; or (iii) covered with a Kapton sheet (25 μm in thickness, DuPont) and an additional glass slide, preheated to the same temperature, for XRD. After 2 additional

https://doi.org/10.1021/acs.chemmater.5c01893
Chem. Mater. 2025, 37, 8809−8821

minutes, the sample was quickly removed to a room-temperature metal surface and was immediately covered by a cold stainless-steel weight (unless uncovered, option i). Upon completely cooling back to room temperature, the weight was removed.

Fourier Transform Infrared Spectroscopy. FT-IR Spectra were measured using a Thermo Fisher Scientific Nicolet iS50 FT-IR spectrometer. A few mg of each binary glass sample (prepared uncovered, see above), were scraped off the glass substrate (using a stainless-steel spatula) and placed in the spectrometer sample holder. Crystalline (as-is) samples of the pure HOIPs were measured as well. Each sample was scanned in the range of 400−4000 cm^{-1}.

SEM-EDS. A few mg of each binary glass sample (prepared uncovered), were scraped off the glass substrate directly onto a carbon tape-coated SEM stub. EDS mapping was performed in the Zeiss Gemini SEM, without carbon-coating the samples. Electron micrographs were acquired using the backscattered electrons (BSE) detector, as the energy of the primary electron beam (for both imaging and EDS mapping) was set to 15 keV.

Stability Measurements. Each Kapton-covered glassy sample was mounted on a plastic XRD holder (Kapton side up) and scanned immediately after preparation. Assuming the first scan for each sample was performed at 0 h (immediately after glass formation), each sample was rescanned after 0.5 h, 12 h, 1 day, 1.5 days, 2 days, 2.5 days, 3 days, 5 days, 1 week, 2 weeks, 1 month, and once again after 6 months.

Mechanical Properties. Uncovered glassy samples were mounted into the nanoindenter and secured using a double-sided adhesive tape. Each sample was indented 20 times at different positions. The maximal load was set to be 25 mN, while the maximal depth was 2500 nm. Before starting the measurement, the indenter was calibrated using a reference silica sample. Before and after each indentation, the tip was cleaned by performing 4 measurements on a reference aluminum surface. The hardness and Young's modulus of each sample were calculated based on the closest 15 values out of the 20 measured. An additional sample of crystalline *S*-NPB was prepared by thermal annealing a glassy *S*-NPB sample on a hot plate, preheated to 100 °C, for 5 min. In this sample, indentation was performed on flat and smooth parts in the sample, representing the exposed (001) facets of the crystal.

Density Measurements. The density of crystalline and glassy *S*-NPB was measured using a gas pycnometer, with N_2 as the medium. SDT alumina crucibles (70 μL) were cleaned by sonicating them for 30 min in acetone, then disposing of the liquid and thoroughly washing them. This process was repeated once more, then twice again with isopropanol, and finally the crucibles were left to dry overnight at 50 °C. Each crucible was accurately weighed, then filled with *S*-NPB powder, and placed on a hot plate preheated to 190 °C. When a complete melting was achieved, as evident by the transformation of all the powder to a liquid, the crucibles were removed from the hot plate and placed on a metal surface for rapid cooling and glass formation. To recrystallize the glass, one crucible was transferred back to the hot plate, this time preheated to 120 °C, and was left to recrystallize for 15 min, until the transparent glass seemed to completely transform to a white solid. Each crucible was inserted in turn to the pycnometer chamber (AccuPyc 1350, 10 cm^3, Malvern Panalytical), then underwent 25 purge cycles, followed by 25 measurement cycles. The N_2 pressure in the chamber was set to be 19.500 psig, and the pressure rate of change used as a stability criterion was 0.0050 psig min^{-1}. The temperature for all the cycles was 20.000 ± 0.003 °C. After the measurements, the crucibles were cleaned again (using the same cleaning process as before), then remeasured empty. The true density of each sample was calculated according to

$$\rho_{true} = \frac{m_{full} - m_{empty}}{V_{full} - V_{empty}} \quad (8)$$

where m and V are the mass and the average volume of the full and empty crucible, respectively.

Optical Properties. The optical absorbance of the samples was measured using a Carry 60 UV−vis spectrophotometer. Each glassy sample, sandwiched between two clean glass slides, was inserted into the spectrophotometer (immediately after preparation) and scanned between 350 and 800 nm for its optical absorbance. Then, each sample was placed back on the hot plate, this time preheated to 100 °C, and left on it for 5 min. The samples were naturally cooled to room temperature, followed by remeasurement of their optical absorbance under the same conditions as before.

■ ASSOCIATED CONTENT

Supporting Information

The Supporting Information is available free of charge at https://pubs.acs.org/doi/10.1021/acs.chemmater.5c01893.

Additional experimental details, including NMR, TGA, XRD, FT-IR, SEM, EDS, XPDF, optical absorption, nanoindentation, and pycnometry results, as well as thermodynamic calculations (PDF)

■ AUTHOR INFORMATION

Corresponding Author

Arad Lang − *Department of Materials Science and Metallurgy, University of Cambridge, Cambridge CB3 0FS, U.K.;* Present Address: Department of Materials Science and Engineering, Technion − Israel Institute of Technology, Haifa 3200003, Israel; orcid.org/0000-0003-3692-7628; Email: al2213@cam.ac.uk

Authors

Chumei Ye − *Department of Materials Science and Metallurgy, University of Cambridge, Cambridge CB3 0FS, U.K.; Cavendish Laboratory, University of Cambridge, Cambridge CB3 0US, U.K.*

Celia Chen − *Department of Materials Science and Metallurgy, University of Cambridge, Cambridge CB3 0FS, U.K.; Cavendish Laboratory, University of Cambridge, Cambridge CB3 0US, U.K.*

Lauren N. McHugh − *Department of Chemistry, University of Liverpool, Liverpool L69 7ZD, U.K.*

Emily V. Shaw − *Department of Materials Science and Metallurgy, University of Cambridge, Cambridge CB3 0FS, U.K.*

Catherine Dejoie − *ESRF - The European Synchrotron Radiation Facility, Grenoble 38043, France;* orcid.org/0000-0003-3313-3515

Giulio I. Lampronti − *Department of Materials Science and Metallurgy, University of Cambridge, Cambridge CB3 0FS, U.K.;* orcid.org/0000-0002-1430-3446

Malvina Constantinou − *Cavendish Laboratory, University of Cambridge, Cambridge CB3 0US, U.K.;* orcid.org/0009-0003-7501-8408

Rachel C. Evans − *Department of Materials Science and Metallurgy, University of Cambridge, Cambridge CB3 0FS, U.K.;* orcid.org/0000-0003-2956-4857

Thomas D. Bennett − *Department of Materials Science and Metallurgy, University of Cambridge, Cambridge CB3 0FS, U.K.; MacDiarmid Institute for Advanced Materials and Nanotechnology, School of Physical and Chemical Sciences, University of Canterbury, Christchurch 8140, New Zealand*

Siân E. Dutton − *Cavendish Laboratory, University of Cambridge, Cambridge CB3 0US, U.K.;* orcid.org/0000-0003-0984-5504

Complete contact information is available at: https://pubs.acs.org/10.1021/acs.chemmater.5c01893

https://doi.org/10.1021/acs.chemmater.5c01893
Chem. Mater. 2025, 37, 8809−8821

Notes

The authors declare no competing financial interest.

■ ACKNOWLEDGMENTS

We acknowledge the European Synchrotron Radiation Facility (ESRF) for the provision of synchrotron radiation facilities under proposal number MA-6548. We would like to thank Dr. David Williamson for kindly providing access to his laboratory's pycnometer. A. Lang acknowledges financial support by the Blavatnik Family Foundation, as part of the Blavatnik Cambridge Postdoctoral Fellowship.

■ REFERENCES

(1) Zhao, Y.; Zhu, K. Organic−Inorganic Hybrid Lead Halide Perovskites for Optoelectronic and Electronic Applications. *Chem. Soc. Rev.* **2016**, *45* (3), 655−689.
(2) Chen, Z.; Turedi, B.; Alsalloum, A. Y.; Yang, C.; Zheng, X.; Gereige, I.; Alsaggaf, A.; Mohammed, O. F.; Bakr, O. M. Single-Crystal MAPbI3 Perovskite Solar Cells Exceeding 21% Power Conversion Efficiency. *ACS Energy Lett.* **2019**, *4* (6), 1258−1259.
(3) Aharon, S.; Cohen, B. E.; Etgar, L. Hybrid Lead Halide Iodide and Lead Halide Bromide in Efficient Hole Conductor Free Perovskite Solar Cell. *J. Phys. Chem. C* **2014**, *118* (30), 17160−17165.
(4) Ono, L. K.; Qi, Y.; Liu, S. Progress toward Stable Lead Halide Perovskite Solar Cells. *Joule* **2018**, *2* (10), 1961−1990.
(5) Zhang, W.; Eperon, G. E.; Snaith, H. J. Metal Halide Perovskites for Energy Applications. *Nat. Energy* **2016**, *1* (6), 16048.
(6) Kim, Y. H.; Cho, H.; Heo, J. H.; Kim, T. S.; Myoung, N. S.; Lee, C. L.; Im, S. H.; Lee, T. W. Multicolored Organic/Inorganic Hybrid Perovskite Light-Emitting Diodes. *Adv. Mater.* **2015**, *27* (7), 1248−1254.
(7) Lin, K.; Xing, J.; Quan, L. N.; de Arquer, F. P. G.; Gong, X.; Lu, J.; Xie, L.; Zhao, W.; Zhang, D.; Yan, C.; Li, W.; Liu, X.; Lu, Y.; Kirman, J.; Sargent, E. H.; Xiong, Q.; Wei, Z. Perovskite Light-Emitting Diodes with External Quantum Efficiency Exceeding 20 per Cent. *Nature* **2018**, *562* (7726), 245−248.
(8) Kim, Y.-H.; Cho, H.; Lee, T.-W. Metal Halide Perovskite Light Emitters. *Proc. Natl. Acad. Sci. U. S. A.* **2016**, *113* (42), 11694−11702.
(9) Liu, X. K.; Xu, W.; Bai, S.; Jin, Y.; Wang, J.; Friend, R. H.; Gao, F. Metal Halide Perovskites for Light-Emitting Diodes. *Nat. Mater.* **2021**, *20* (1), 10−21.
(10) Tian, W.; Zhou, H.; Li, L. Hybrid Organic−Inorganic Perovskite Photodetectors. *Small* **2017**, *13* (41), 1702107.
(11) Kakavelakis, G.; Gedda, M.; Panagiotopoulos, A.; Kymakis, E.; Anthopoulos, T. D.; Petridis, K. Metal Halide Perovskites for High-Energy Radiation Detection. *Adv. Sci.* **2020**, *7* (22), 2002098.
(12) Wu, H.; Ge, Y.; Niu, G.; Tang, J. Metal Halide Perovskites for X-Ray Detection and Imaging. *Matter* **2021**, *4* (1), 144−163.
(13) Zhang, B.; Xue, B.; Xiao, S.; Wang, X. Chemical Stability of Metal Halide Perovskite Detectors. *Inorganics* **2024**, *12* (2), 52.
(14) Luo, S.; Daoud, W. Crystal Structure Formation of CH3NH3PbI3-XClx Perovskite. *Materials* **2016**, *9* (3), 123.
(15) Ong, K. P.; Goh, T. W.; Xu, Q.; Huan, A. Structural Evolution in Methylammonium Lead Iodide CH3NH3PbI3. *J. Phys. Chem. A* **2015**, *119* (44), 11033−11038.
(16) Burger, S.; Ehrenreich, M. G.; Kieslich, G. Tolerance Factors of Hybrid Organic−Inorganic Perovskites: Recent Improvements and Current State of Research. *J. Mater. Chem. A* **2018**, *6* (44), 21785−21793.
(17) Mao, L.; Stoumpos, C. C.; Kanatzidis, M. G. Two-Dimensional Hybrid Halide Perovskites: Principles and Promises. *J. Am. Chem. Soc.* **2019**, *141* (3), 1171−1190.
(18) Zhang, F.; Lu, H.; Tong, J.; Berry, J. J.; Beard, M. C.; Zhu, K. Advances in Two-Dimensional Organic−Inorganic Hybrid Perovskites. *Energy Environ. Sci.* **2020**, *13* (4), 1154−1186.
(19) Dou, L.; Wong, A. B.; Yu, Y.; Lai, M.; Kornienko, N.; Eaton, S. W.; Fu, A.; Bischak, C. G.; Ma, J.; Ding, T.; Ginsberg, N. S.; Wang, L.-W.; Alivisatos, A. P.; Yang, P. Atomically Thin Two-Dimensional Organic-Inorganic Hybrid Perovskites. *Science* **2015**, *349* (6255), 1518−1521.
(20) Gu, H.; Xia, J.; Liang, C.; Chen, Y.; Huang, W.; Xing, G. Phase-Pure Two-Dimensional Layered Perovskite Thin Films. *Nat. Rev. Mater.* **2023**, *8* (8), 533−551.
(21) Thrithamarassery Gangadharan, D.; Ma, D. Searching for Stability at Lower Dimensions: Current Trends and Future Prospects of Layered Perovskite Solar Cells. *Energy Environ. Sci.* **2019**, *12* (10), 2860−2889.
(22) Yang, D.; Zhao, B.; Yang, T.; Lai, R.; Lan, D.; Friend, R. H.; Di, D. Toward Stable and Efficient Perovskite Light-Emitting Diodes. *Adv. Funct. Mater.* **2022**, *32* (9), 2109495.
(23) Quarti, C.; Marchal, N.; Beljonne, D. Tuning the Optoelectronic Properties of Two-Dimensional Hybrid Perovskite Semiconductors with Alkyl Chain Spacers. *J. Phys. Chem. Lett.* **2018**, *9* (12), 3416−3424.
(24) Pandey, M.; Jacobsen, K. W.; Thygesen, K. S. Band Gap Tuning and Defect Tolerance of Atomically Thin Two-Dimensional Organic-Inorganic Halide Perovskites. *J. Phys. Chem. Lett.* **2016**, *7* (21), 4346−4352.
(25) Huo, C.; Cai, B.; Yuan, Z.; Ma, B.; Zeng, H. Two-Dimensional Metal Halide Perovskites: Theory, Synthesis, and Optoelectronics. *Small Methods* **2017**, *1* (3), 1600018.
(26) Yusoff, A.; Bin Mohd, R.; Nazeeruddin, M. K. Low-Dimensional Perovskites: From Synthesis to Stability in Perovskite Solar Cells. *Adv. Energy Mater.* **2018**, *8* (26), 1702073.
(27) Lan, C.; Zhou, Z.; Wei, R.; Ho, J. C. Two-Dimensional Perovskite Materials: From Synthesis to Energy-Related Applications. *Mater. Today Energy* **2019**, *11*, 61−82.
(28) Zheng, K.; Pullerits, T. Two Dimensions Are Better for Perovskites. *J. Phys. Chem. Lett.* **2019**, *10* (19), 5881−5885.
(29) Ye, C.; McHugh, L. N.; Chen, C.; Dutton, S. E.; Bennett, T. D. Glass Formation in Hybrid Organic-Inorganic Perovskites. *Angew. Chem., Int. Ed.* **2023**, *62* (28), No. e202302406.
(30) Singh, A.; Mitzi, D. B. Emergence of Melt and Glass States of Halide Perovskite Semiconductors. *Nat. Rev. Mater.* **2025**, *10* (10), 211−227.
(31) Shaw, B. K.; Hughes, A. R.; Ducamp, M.; Moss, S.; Debnath, A.; Sapnik, A. F.; Thorne, M. F.; McHugh, L. N.; Pugliese, A.; Keeble, D. S.; Chater, P.; Bermudez-Garcia, J. M.; Moya, X.; Saha, S. K.; Keen, D. A.; Coudert, F.-X.; Blanc, F.; Bennett, T. D. Melting of Hybrid Organic−Inorganic Perovskites. *Nat. Chem.* **2021**, *13* (8), 778−785.
(32) Shaw, B. K.; Castillo-Blas, C.; Thorne, M. F.; Ríos Gómez, M. L.; Forrest, T.; Lopez, M. D.; Chater, P. A.; McHugh, L. N.; Keen, D. A.; Bennett, T. D. Principles of Melting in Hybrid Organic−Inorganic Perovskite and Polymorphic ABX_3 Structures. *Chem. Sci.* **2022**, *13* (7), 2033−2042.
(33) Singh, A.; Crace, E.; Xie, Y.; Mitzi, D. B. A Two-Dimensional Lead-Free Hybrid Perovskite Semiconductor with Reduced Melting Temperature. *Chem. Commun.* **2023**, *59* (53), 8302−8305.
(34) Li, T.; Dunlap-Shohl, W. A.; Reinheimer, E. W.; Le Magueres, P.; Mitzi, D. B. Melting Temperature Suppression of Layered Hybrid Lead Halide Perovskites *via* Organic Ammonium Cation Branching. *Chem. Sci.* **2019**, *10* (4), 1168−1175.
(35) Vargas, B.; Rodríguez-López, G.; Solis-Ibarra, D. The Emergence of Halide Layered Double Perovskites. *ACS Energy Lett.* **2020**, *5* (11), 3591−3608.
(36) Wang, W.; Liu, C.-D.; Fan, C.-C.; Fu, X.-B.; Jing, C.-Q.; Jin, M.-L.; You, Y.-M.; Zhang, W. Rational Design of 2D Metal Halide Perovskites with Low Congruent Melting Temperature and Large Melt-Processable Window. *J. Am. Chem. Soc.* **2024**, *146* (13), 9272−9284.
(37) Hadi, A.; Schlichtmann, R. L.; Milot, M. I.; Slobidsky, J.; Wilsey, M.; Verburg, A.; Chen, Y.; Hamdeh, U. H.; Ryan, B. J.; Boote, B.; Vela, J.; Panthani, M. G. Melt-Processed Halide Perovskite Thin Films from a Two-Dimensional Ruddlesden−Popper Phase Precursor. *J. Phys. Chem. Lett.* **2023**, *14* (22), 5194−5202.

https://doi.org/10.1021/acs.chemmater.5c01893
Chem. Mater. 2025, 37, 8809−8821

(38) Wang, W.; Zhang, J.-M.; Jin, M.-L.; Jing, C.-Q.; Zhang, W. A 9R-like 2D Hybrid Metal Halide with Remarkably Low Melting Temperature. *Chem. Commun.* **2024**, *61* (2), 362−365.
(39) Singh, A.; Jana, M. K.; Mitzi, D. B. Reversible Crystal−Glass Transition in a Metal Halide Perovskite. *Adv. Mater.* **2021**, *33* (3), 2005868.
(40) Wang, W.; Liu, C.; Fan, C.; Zhang, W. Reversible Glass-Crystal Transition in a New Type of 2D Metal Halide Perovskites. *Adv. Funct. Mater.* **2024**, *34* (44), 2407143.
(41) Ye, C.; Lampronti, G. I.; McHugh, L. N.; Castillo-Blas, C.; Kono, A.; Chen, C.; Robertson, G. P.; Nagle-Cocco, L. A. V.; Xu, W.; Stranks, S. D.; Martinez, V.; Brekalo, I.; Karadeniz, B.; Užarević, K.; Xue, W.; Kolodzeiski, P.; Das, C.; Chater, P.; Keen, D. A.; Dutton, S. E.; Bennett, T. D. Mechanochemically-Induced Glass Formation from Two-Dimensional Hybrid Organic-Inorganic Perovskites. *Chem. Sci.* **2024**, *15* (19), 7198−7205.
(42) Singh, A.; Dayton, D.; Ladd, D. M.; Reuveni, G.; Paluch, P.; Montagne, L.; Mars, J.; Yaffe, O.; Toney, M.; Manjunatha Reddy, G. N.; Mitzi, D. B. Local Structure in Crystalline, Glass and Melt States of a Hybrid Metal Halide Perovskite. *J. Am. Chem. Soc.* **2024**, *146* (37), 25656.
(43) Jana, M. K.; Song, R.; Liu, H.; Khanal, D. R.; Janke, S. M.; Zhao, R.; Liu, C.; Valy Vardeny, Z.; Blum, V.; Mitzi, D. B. Organic-to-Inorganic Structural Chirality Transfer in a 2D Hybrid Perovskite and Impact on Rashba-Dresselhaus Spin-Orbit Coupling. *Nat. Commun.* **2020**, *11* (1), 4699.
(44) Ye, C.; McHugh, L. N.; Florian, P.; Yu, R.; Castillo-Blas, C.; Chen, C.; Lang, A.; Dai, Y.; Hou, J.; Keen, D. A.; Dutton, S. E.; Bennett, T. D. Structural Dynamics of Melting and Glass Formation in a Two-Dimensional Hybrid Perovskite. *Nat. Commun.* **2025**, *16* (1), 7696.
(45) Singh, A.; Mitzi, D. B. Crystallization Kinetics in a Glass-Forming Hybrid Metal Halide Perovskite. *ACS Mater. Lett.* **2022**, *4* (9), 1840−1847.
(46) Wang, W.; Liu, C.-D.; Han, X.-B.; Jing, C.-Q.; Chai, C.-Y.; Fan, C.-C.; Jin, M.-L.; Zhang, J.-M.; Zhang, W. Photoluminescence Switching and Non-Volatile Memory in Hybrid Metal-Halide Phase-Change Materials. *ACS Mater. Lett.* **2024**, *6* (1), 203−211.
(47) Zhou, B.; Yan, D. Glassy Inorganic-Organic Hybrid Materials for Photonic Applications. *Matter* **2024**, *7* (6), P1950−1976.
(48) Blanc, W.; Gyu Choi, Y.; Zhang, X.; Nalin, M.; Richardson, K. A.; Righini, G. C.; Ferrari, M.; Jha, A.; Massera, J.; Jiang, S.; Ballato, J.; Petit, L. The Past, Present and Future of Photonic Glasses: A Review in Homage to the United Nations International Year of Glass 2022. *Prog. Mater. Sci.* **2023**, *134*, 101084.
(49) Ballato, J.; Ebendorff-Heidepriem, H.; Zhao, J.; Petit, L.; Troles, J. Glass and Process Development for the Next Generation of Optical Fibers: A Review. *Fibers* **2017**, *5* (1), 11.
(50) Kang, S.; Fu, Y.; Gu, H.; Lin, C. Chalcogenide Glass for Thermoelectric Application. *J. Non-Cryst. Solids:X* **2022**, *15*, 100111.
(51) Gonçalves, A. P.; Lopes, E. B.; Delaizir, G.; Vaney, J. B.; Lenoir, B.; Piarristeguy, A.; Pradel, A.; Monnier, J.; Ochin, P.; Godart, C. Semiconducting Glasses: A New Class of Thermoelectric Materials? *J. Solid State Chem.* **2012**, *193*, 26−30.
(52) Peng, Q.-P.; Wei, J.-H.; He, Z.-L.; Luo, J.-B.; Chen, J.-H.; Zhang, Z.-Z.; Guo, X.-X.; Kuang, D.-B. *In Situ* Crystallization of $CsPbBr_3$ Nanocrystals within a Melt-Quenched Glassy Coordination Polymer. *ACS Nano* **2025**, *19* (5), 5295−5304.
(53) Hou, J.; Chen, P.; Shukla, A.; Krajnc, A.; Wang, T.; Li, X.; Doasa, R.; Tizei, L. H. G.; Chan, B.; Johnstone, D. N.; Lin, R.; Schülli, T. U.; Martens, I.; Appadoo, D.; Ari, M. S.; Wang, Z.; Wei, T.; Lo, S.-C.; Lu, M.; Li, S.; Namdas, E. B.; Mali, G.; Cheetham, A. K.; Collins, S. M.; Chen, V.; Wang, L.; Bennett, T. D. Liquid-Phase Sintering of Lead Halide Perovskites and Metal-Organic Framework Glasses. *Science* **2021**, *374* (6567), 621−625.
(54) Sohn, H. Y.; Sridhar, S. Descriptions of High-Temperature Metallurgical Processes. In *Fundamentals of Metallurgy*; Elsevier, 2005; pp. 3−37. DOI: 10.1533/9781845690946.1.3.
(55) Anantharaman, T. R.; Suryanarayana, C. Review: A Decade of Quenching from the Melt. *J. Mater. Sci.* **1971**, *6* (8), 1111−1135.
(56) Watcharatpong, T.; Crespy, D.; Kadota, K.; Wang, S.-M.; Kongpatpanich, K.; Horike, S. Alloying One-Dimensional Coordination Polymers To Create Ductile Materials. *J. Am. Chem. Soc.* **2024**, *146* (33), 23412.
(57) Longley, L.; Collins, S. M.; Zhou, C.; Smales, G. J.; Norman, S. E.; Brownbill, N. J.; Ashling, C. W.; Chater, P. A.; Tovey, R.; Schönlieb, C.-B.; Headen, T. F.; Terrill, N. J.; Yue, Y.; Smith, A. J.; Blanc, F.; Keen, D. A.; Midgley, P. A.; Bennett, T. D. Liquid Phase Blending of Metal-Organic Frameworks. *Nat. Commun.* **2018**, *9* (1), 2135.
(58) Lang, A.; Chen, C.; Ye, C.; McHugh, L. N.; Chua, X. W.; Stranks, S. D.; Dutton, S. E.; Bennett, T. D. Melt Alloying of Two-Dimensional Hybrid Perovskites: Composition-Dependence of Thermal and Optical Properties. *J. Am. Chem. Soc.* **2024**, *146* (49), 33945.
(59) Brandon, D. G.; Kaplan, W. D. *Microstructural Characterization of Materials*, 2nd ed.; John Wiley & Sons, Ltd, 2008.
(60) Mingueza-Verdejo, P.; Hernández-Garrido, J. C.; Vidal-Moya, A.; Oliver-Meseguer, J.; Leyva-Pérez, A. Zeolites Catalyze the Halogen Exchange Reaction of Alkyl Halides. *Catal. Sci. Technol.* **2023**, *13* (8), 2308−2316.
(61) Pace, R. D.; Regmi, Y. The Finkelstein Reaction: Quantitative Reaction Kinetics of an SN2 Reaction Using Nonaqueous Conductivity. *J. Chem. Educ.* **2006**, *83* (9), 1344.
(62) Sidebottom, D. L. Fifty Years of Fragility: A View from the Cheap Seats. *J. Non-Cryst. Solids* **2019**, *524*, 119641.
(63) Huang, D.; McKenna, G. B. New Insights into the Fragility Dilemma in Liquids. *J. Chem. Phys.* **2001**, *114* (13), 5621−5630.
(64) Alba-Simionesco, C.; Tarjus, G. A Perspective on the Fragility of Glass-Forming Liquids. *J. Non-Cryst. Solids:X* **2022**, *14*, 100100.
(65) Debenedetti, P. G.; Stillinger, F. H. Supercooled Liquids and the Glass Transition. *Nature* **2001**, *410* (6825), 259−267.
(66) Crowley, K. J.; Zografi, G. The Use of Thermal Methods for Predicting Glass-Former Fragility. *Thermochim. Acta* **2001**, *380* (2), 79−93.
(67) Huang, C.-C.; Du, M.-X.; Zhang, B.-Q.; Liu, C.-Y. Glass Transition Temperatures of Copolymers: Molecular Origins of Deviation from the Linear Relation. *Macromolecules* **2022**, *55* (8), 3189−3200.
(68) Moynihan, C. T.; Easteal, A. J.; Wilder, J.; Tucker, J. Dependence of the Glass Transition Temperature on Heating and Cooling Rate. *J. Phys. Chem.* **1974**, *78* (26), 2673−2677.
(69) Aji, D. P. B.; Johari, G. P. Fictive Temperature, Structural Relaxation, and Reality of Residual Entropy. *J. Phys. Chem. B* **2010**, *114* (29), 9578−9585.
(70) Hirooka, M.; Kato, T. Glass Transition Temperature and Sequential Structure of Equimolar Copolymers. *J. Polym. Sci.: Polym. Lett. Ed.* **1974**, *12* (1), 31−37.
(71) Qiao, A.; Bennett, T. D.; Tao, H.; Krajnc, A.; Mali, G.; Doherty, C. M.; Thornton, A. W.; Mauro, J. C.; Greaves, G. N.; Yue, Y. A Metal-Organic Framework with Ultrahigh Glass-Forming Ability. *Sci. Adv.* **2018**, *4* (3), No. eaao6827.
(72) McCarron, J.; Turner, B.; McHugh, L. N. Hybrid Framework Materials: Next-Generation Engineering Materials. *Adv. Eng. Mater.* **2025**, *27* (9), 2402554.
(73) Angelo, R. J.; Ikeda, R. M.; Wallach, M. L. Multiple Glass Transitions of Block Polymers. *Polymer* **1965**, *6* (3), 141−156.
(74) Chen, C.; Lang, A.; Shaw, E. Towards Stable Binary Hybrid Perovskite Glasses: A Combined Long- and Short-Range Order Structural Study. **2028**. .
(75) Fitch, A.; Dejoie, C.; Covacci, E.; Confalonieri, G.; Grendal, O.; Claustre, L.; Guillou, P.; Kieffer, J.; de Nolf, W.; Petitdemange, S.; Ruat, M.; Watier, Y. ID22 − the High-Resolution Powder-Diffraction Beamline at ESRF. *J. Synchrotron Radiat.* **2023**, *30* (5), 1003−1012.
(76) Qiao, C.-K.; Wei, J.-W.; Chen, L. An Overview of the Compton Scattering Calculation. *Crystals* **2021**, *11* (5), 525.

(77) Narayanaswamy, O. S. A Model of Structural Relaxation in Glass. *J. Am. Ceram. Soc.* **1971**, *54* (10), 491−498.
(78) Zhang, Z.; Tang, Y.; Ying, Y.; Guo, J.; Gan, M.; Jiang, Y.; Xing, C.; Pan, S.; Xu, M.; Zhou, Y.; Zhang, H.; Leung, C. W.; Huang, H.; Mak, C. L.; Fei, L. Multistep Nucleation Visualized during Solid-State Crystallization. *Mater. Horiz.* **2022**, *9* (6), 1670−1678.
(79) Greaves, G. N.; Sen, S. Inorganic Glasses, Glass-Forming Liquids and Amorphizing Solids. *Adv. Phys.* **2007**, *56* (1), 1−166.
(80) Zanotto, E. D.; Mauro, J. C. The Glassy State of Matter: Its Definition and Ultimate Fate. *J. Non-Cryst. Solids* **2017**, *471*, 490−495.
(81) Toso, S.; Gushchina, I.; Oliver, A. G.; Manna, L.; Kuno, M. Are Mixed-Halide Ruddlesden−Popper Perovskites Really Mixed? *ACS Energy Lett.* **2022**, *7* (12), 4242−4247.
(82) Hoke, E. T.; Slotcavage, D. J.; Dohner, E. R.; Bowring, A. R.; Karunadasa, H. I.; McGehee, M. D. Reversible Photo-Induced Trap Formation in Mixed-Halide Hybrid Perovskites for Photovoltaics. *Chem. Sci.* **2015**, *6* (1), 613−617.
(83) Draguta, S.; Sharia, O.; Yoon, S. J.; Brennan, M. C.; Morozov, Y. V.; Manser, J. S.; Kamat, P. V.; Schneider, W. F.; Kuno, M. Rationalizing the Light-Induced Phase Separation of Mixed Halide Organic−Inorganic Perovskites. *Nat. Commun.* **2017**, *8* (1), 200.
(84) Oliver, W. C.; Pharr, G. M. Nanoindentation in Materials Research: Past, Present, and Future. *MRS Bull.* **2010**, *35* (11), 897−907.
(85) Lucca, D. A.; Herrmann, K.; Klopfstein, M. J. N. Measuring Methods and Applications. *CIRP Ann.* **2010**, *59* (2), 803−819.
(86) Fang, Q.; Pang, Z.; Ai, Q.; Liu, Y.; Zhai, T.; Steinbach, D.; Gao, G.; Zhu, Y.; Li, T.; Lou, J. Superior Mechanical Properties of Multilayer Covalent-Organic Frameworks Enabled by Rationally Tuning Molecular Interlayer Interactions. *Proc. Natl. Acad. Sci. U. S. A.* **2023**, *120* (15), No. e2208676120.
(87) Liu, J.; Qin, H.; Liu, Y. Multi-Scale Structure−Mechanical Property Relations of Graphene-Based Layer Materials. *Materials* **2021**, *14* (16), 4757.
(88) Makuła, P.; Pacia, M.; Macyk, W. How To Correctly Determine the Band Gap Energy of Modified Semiconductor Photocatalysts Based on UV-Vis Spectra. *J. Phys. Chem. Lett.* **2018**, *9* (23), 6814−6817.
(89) Lang, A.; Polishchuk, I.; Seknazi, E.; Feldmann, J.; Katsman, A.; Pokroy, B. Bioinspired Molecular Bridging in a Hybrid Perovskite Leads to Enhanced Stability and Tunable Properties. *Adv. Funct. Mater.* **2020**, *30* (42), 2005136.
(90) Noh, J. H.; Im, S. H.; Heo, J. H.; Mandal, T. N.; Seok, S. I. Chemical Management for Colorful, Efficient, and Stable Inorganic−Organic Hybrid Nanostructured Solar Cells. *Nano Lett.* **2013**, *13* (4), 1764−1769.
(91) Jong, U.-G.; Yu, C.-J.; Ri, J.-S.; Kim, N.-H.; Ri, G.-C. Influence of Halide Composition on the Structural, Electronic, and Optical Properties of Mixed CH3NH3Pb(I1−xBrx)3 Perovskites Calculated Using the Virtual Crystal Approximation Method. *Phys. Rev. B* **2016**, *94* (12), 125139.
(92) Hill, R. Energy-Gap Variations in Semiconductor Alloys. *J. Phys. C: solid State Phys.* **1974**, *7* (3), 521−526.
(93) Atourki, L.; Vega, E.; Marí, B.; Mollar, M.; Ait Ahsaine, H.; Bouabid, K.; Ihlal, A. Role of the Chemical Substitution on the Structural and Luminescence Properties of the Mixed Halide Perovskite Thin MAPbI3−xBrx ($0 \leq x \leq 1$) Films. *Appl. Surf. Sci.* **2016**, *371*, 112−117.
(94) Wang, M.; Fei, G. T.; Zhang, Y. G.; Kong, M. G.; Zhang, L. D. Tunable and Predetermined Bandgap Emissions in Alloyed ZnS_xSe_{1-x} Nanowires. *Adv. Mater.* **2007**, *19* (24), 4491−4494.
(95) Soper, A. K. *GudrunN and GudrunX: programs for correcting raw neutron and X-ray diffraction data to differential scattering cross section*; Science & Technology Facilities Council, 2011.
(96) Keen, D. A. Total Scattering and the Pair Distribution Function in Crystallography. *Crystallogr. Rev.* **2020**, *26* (3), 143−201.
(97) Keen, D. A. A Comparison of Various Commonly Used Correlation Functions for Describing Total Scattering. *J. Appl. Crystallogr.* **2001**, *34* (2), 172−177.
(98) Stevens, E. D. Thermal Diffuse Scattering Corrections for Single-Crystal Integrated Intensity Measurement. *Acta Crystallogr., Sect. A: Found. Adv.* **1974**, *30* (2), 184−189.

https://doi.org/10.1021/acs.chemmater.5c01893
Chem. Mater. 2025, 37, 8809−8821